Terahertz spectroscopy for all-optical spintronic characterization of the spin-Hall-effect metals Pt, W and Cu$_{80}$Ir$_{20}$

T S Seifert[1,2,3], **N M Tran**[4], **O Gueckstock**[1], **S M Rouzegar**[1], **L Nadvornik**[1,2], **S Jaiswal**[5,6], **G Jakob**[5,7], **V V Temnov**[4], **M Münzenberg**[8], **M Wolf**[1], **M Kläui**[5,7] and **T Kampfrath**[1,2]

[1] Department of Physical Chemistry, Fritz Haber Institute of the Max Planck Society, 14195 Berlin, Germany
[2] Department of Physics, Freie Universität Berlin, 14195 Berlin, Germany
[3] Department of Materials, Eidgenössische Technische Hochschule Zürich, 8093 Zürich, Switzerland
[4] Institut des Molécules et Matériaux du Mans, UMR CNRS 6283, Le Mans Université, 72085 Le Mans, France
[5] Institute of Physics, Johannes Gutenberg University Mainz, 55099 Mainz, Germany
[6] Singulus Technologies AG, 63796 Kahl am Main, Germany
[7] Graduate School of Excellence Materials Science in Mainz, 55128 Mainz, Germany
[8] Institut für Physik, Universität Greifswald, 17489 Greifswald, Germany

E-mail: tobias.kampfrath@fu-berlin.de

Abstract

Identifying materials with an efficient spin-to-charge conversion is crucial for future spintronic applications. In this respect, the spin Hall effect is a central mechanism as it allows for the interconversion of spin and charge currents. Spintronic material research aims at maximizing its efficiency, quantified by the spin Hall angle Θ_{SH} and the spin-current relaxation length λ_{rel}. We develop an all-optical contact-free method with large sample throughput that allows us to extract Θ_{SH} and λ_{rel}. Employing terahertz spectroscopy and an analytical model, magnetic metallic heterostructures involving Pt, W and Cu$_{80}$Ir$_{20}$ are characterized in terms of their optical and spintronic properties. The validity of our analytical model is confirmed by the good agreement with literature DC values. For the samples considered here, we find indications that the interface plays a minor role for the spin-current transmission. Our findings establish terahertz emission spectroscopy as a reliable tool complementing the spintronics workbench.

Keywords: terahertz emission spectroscopy, terahertz transmission spectroscopy, ultrafast spintronics, ultrafast spincaloritronics

S Supplementary material for this article is available online

(Some figures may appear in colour only in the online journal)

J. Phys. D: Appl. Phys. **51** (2018) 364003

T S Seifert *et al*

1. Introduction

Using the electron spin to replace some parts of conventional electronics based on charge dynamics is the goal of spintronics research [5]. Its large potential for future information technology is highlighted by recently developed competitive spintronic applications such as spin-transfer- and spin–orbit-torque magnetic random-access memory [6–8]. Driven by fundamental and material-science research at the same time, future progress in spintronics crucially relies on the identification of materials with efficient spin-to-charge-current conversion.

Central effects in this regard are the spin Hall effect (SHE) and its inverse (ISHE) which allow for an interconversion of spin and charge currents [9, 10]. The efficiency of this process can be quantified by the product of the spin Hall angle Θ_{SH} and the spin-current relaxation length λ_{rel}. To identify materials with maximum Θ_{SH} and λ_{rel}, one needs to be able to screen many material candidates efficiently and accordingly optimize spintronic device parameters. To this end, a fast, reliable and straightforward characterization method is thus a key to realize future spin-based applications.

So far, most works relied on electrical measurements which require microstructuring and electrical contacting of the samples [11–14]. This procedure is costly, time-consuming and may complicate data interpretation due to additional contact resistance [15]. Other established techniques such as spin-Seebeck-effect measurements do not require microstructuring but still rely on electrical contacting [39]. Recently, non-contact methods have been developed which are based on inductive coupling between a microwave waveguide and the spintronic sample [16] or on magnetooptically detected ferromagnetic resonance [17].

Here, we present an all-optical scheme using terahertz (THz) emission spectroscopy (TES) of metallic heterostructures together with a detailed analysis of how to extract the key quantities Θ_{SH} and λ_{rel}. The operational principle is shown in figure 1(a): The inversion-asymmetric sample is excited by a femtosecond near-infrared pump pulse, thereby driving an ultrafast spin current from the FM into the NM layer. This process can be considered as an ultrafast version of the spin-dependent Seebeck effect. In the NM layer, the ISHE converts the longitudinal spin flow into a transverse, in-plane charge current [18–21]. The sub-picosecond transverse charge-current burst leads to the emission of a THz electromagnetic pulse into the optical far-field where it is detected by electrooptic (EO) sampling [22, 23]. This scenario can also be considered as a realization of the spin-galvanic effect [24].

It is worth noting that THz emission by spintronic multilayers consisting of nanometer-thick ferromagnetic (FM) and nonmagnetic (NM) metals has led to the development of efficient THz emitters [19, 25–29] which are capable of providing a broadband and continuous spectrum from 1 to 30 THz without gaps (for details see [19]). In addition, we recently found agreement between the amplitude of the THz field emitted from FM|NM bilayers and the intrinsic spin-Hall conductivity of the employed NM material [19]. This observation is, however, surprising because Θ_{SH} and λ_{rel} can
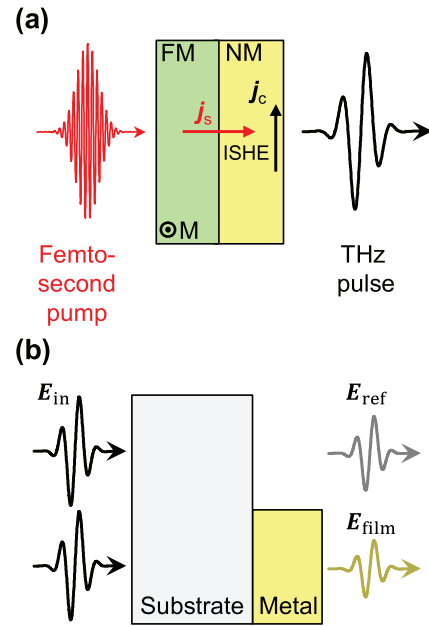
Figure 1. Schematic of the experiments. (a) Terahertz emission experiment. A femtosecond near-infrared pump pulse excites electrons in both the ferromagnetic (FM, in-plane magnetization *M*) and non-magnetic (NM) metal layer. Due to the asymmetry of the heterostructure, a spin current j_s is injected from the FM into the NM material where it is converted into an in-plane charge current j_c by the inverse spin Hall effect (ISHE). The sub-picosecond charge-current burst leads to the emission of a terahertz (THz) pulse into the optical far-field. (b) Terahertz transmission experiment. A THz transient E_{in} is incident onto either the bare substrate or onto the substrate coated by a thin metal film. By comparing the two transmitted waveforms E_{ref} and E_{film}, the metal conductivity at THz frequencies is determined.

strongly depend on the electron energy [30, 31]. Moreover, the spin-current-injection efficiency is material- and interface-dependent [32, 33]. These intriguing issues require a more detailed study to establish TES of magnetic heterostructures [34–37] as a reliable spintronic characterization tool. In the following, we focus on two familiar spintronic metals, namely platinum (Pt) and tungsten (W), as well as a new and promising copper-iridium alloy $Cu_{80}Ir_{20}$ ([38, 39]).

2. Theoretical background

In analogy to DC-spin-pumping experiments [12], we describe the in-plane sheet charge-current density J_c in the NM layer by a simple model which yields [19, 20]

$$ J_c = \frac{A F_{inc}}{d} j_s^0 \cdot \lambda_{rel} \tanh \frac{d_{NM}}{2\lambda_{rel}} \cdot \Theta_{SH}. \quad (1) $$

Here, *A* denotes the absorbed fraction of the incident pump-pulse fluence F_{inc} (the latter being constant for all measurements throughout this work), *d* is the entire metal thickness, j_s^0 is the spin-current density (per pump-pulse excitation density) injected through the FM/NM interface into the NM layer, d_{NM} is the NM layer thickness, λ_{rel} is the relaxation length of the ultrafast spin-current, and Θ_{SH} is the spin Hall angle.

(a)

(b)

(c)

(d)
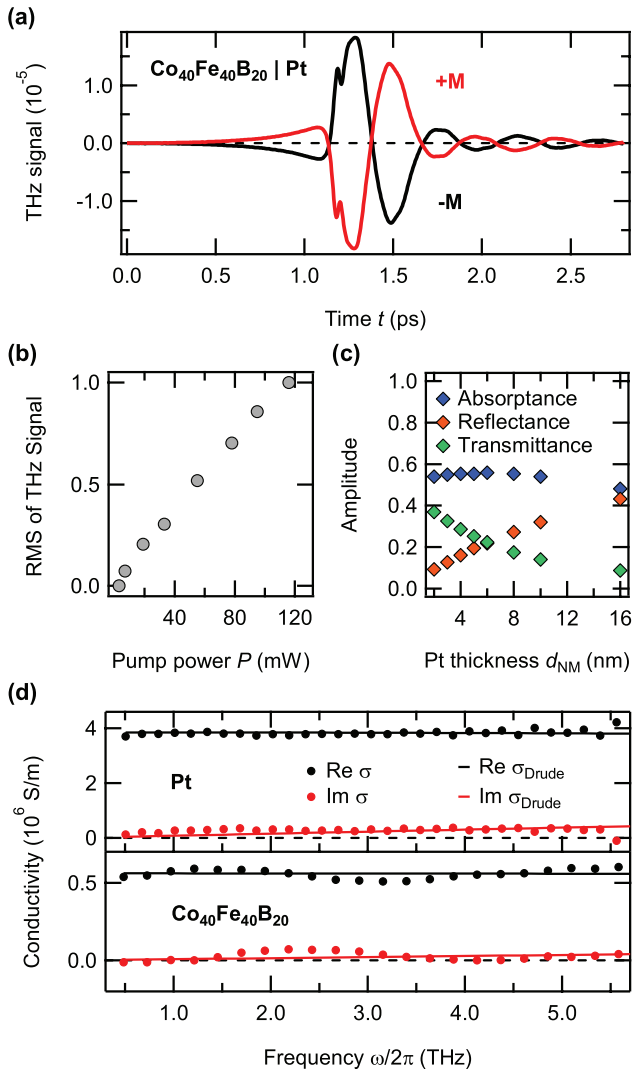
Figure 2. Typical THz-emission raw data and sample characterization. (a) THz-emission signal measured from a $C_{40}F_{40}B_{20}(3\,\text{nm})|Pt(3\,\text{nm})$ bilayer for two opposite orientations of the sample magnetization ($\pm M$). (b) Normalized pump-power dependence of the THz-signal amplitude (RMS) for one orientation of the sample magnetization. (c) Pump-light absorptance, transmittance and reflectance as function of the Pt-layer thickness. (d) Frequency-dependent THz conductivities measured by THz-transmission experiments (black and red dots) along with fits obtained by the Drude model (black and red solid lines).

Equation (1) accounts for the photoinduced injection of the spin current into the NM layer (first term), the multiple spin-current reflections in the NM layer (second term) and the ISHE (last term). For simplicity, we assume a spin-current reflection amplitude of unity at the NM/air and NM/FM interfaces. Moreover, the spin- and energy-dependent electron transmission [32, 33] of the FM/NM interface is assumed to be approximately independent of the NM material. This assumption is supported by our previous work in which a strong correlation between THz-signal amplitude and the spin Hall conductivity of the NM layer was found (see figure 2 in [19]). Since the currents are driven by linear absorption of pump photons (see figure 2(b)), we assume that the sheet charge-current density scales linearly with the pump-pulse excitation density A/d.

Finally, to determine the resulting THz electric field, we assume a normally incident plane-wave-like pump pulse and a sufficiently thin metal film (total metal thickness d minor compared to attenuation length and wavelength of the THz field within the metal). Under these assumptions, the THz electric field directly behind the sample reads [19, 20]

$$E_{\text{THz}}(\omega) = \frac{eZ_0}{n_1 + n_2 + Z_0 \int_0^d \text{d}z\, \sigma(\omega, z)} J_c(\omega). \quad (2)$$

Here, n_1 and $n_2 \approx 1$ are the refractive indices of substrate and air, respectively, $-e$ denotes the electron charge, $Z_0 \approx 377\,\Omega$ is the vacuum impedance, and σ is the z-dependent metal conductivity at THz frequencies.

It is important to emphasize that the derivation of equation (2) relies on a collimated pump beam with a diameter much larger than all THz wavelengths considered. Therefore, the THz beam behind the sample can be approximated by a plane wave. This condition is not fulfilled in our experiment (see below) where the pump focus is substantially smaller than the detected THz wavelengths, which easily exceed 100 μm. However, as shown in the supplementary material (stacks.iop.org/JPhysD/51/364003/mmedia), equation (2) remains valid within a relative error of less than 3% because the apertures of optical elements after the sample reduce the divergence angle of the THz beam to less than 20° with respect to the optical axis.

Equations (1) and (2) provide the key to determine Θ_{SH} and λ_{rel} and naturally take us to the following three-step procedure: First, we characterize the involved metals in terms of their parameters unrelated to spintronics, namely A and σ (see figure 1(b)). Second, we extract λ_{rel} by varying the NM layer thickness in a THz-emission experiment (see figure 1(a)). Third, we address the spin-current transmission of the FM/NM interface. Eventually, the relative spin Hall angle Θ_{SH} is determined by a reference measurement using the widely studied metal Pt as the NM layer [40].

3. Experimental details

We employ femtosecond near-infrared laser pulses (central wavelength of 800 nm, duration of 10 fs, energy of 2.5 nJ, repetition rate of 80 MHz) from a Ti:sapphire laser oscillator to excite the sample under study (see figure 1(a)). In the THz-emission experiment (figure 1(a)), the pump beam is focused onto the sample (spot size of 22 μm full width at half-maximum of the intensity). The emitted THz pulse is detected by EO sampling [22, 23] in a standard 1-mm-thick ZnTe crystal using a copropagating femtosecond near-infrared pulse derived from the same laser. To saturate the sample magnetization in the sample plane, an external field of 10 mT is applied. All measurements are carried out in a dry nitrogen atmosphere.

For the THz conductivity measurements [41] (figure 1(b)), the femtosecond pump pulses are replaced by broadband THz pulses generated in a spintronic THz emitter [19]. We measure the transmission of the THz pulse through the metallic sample film on the substrate and through a part of the substrate free of any metal (see figure 1(b) and supplementary material for

J. Phys. D: Appl. Phys. **51** (2018) 364003

T S Seifert *et al*

Table 1. Overview of samples used for THz-emission measurements together with the corresponding reference samples. Numbers in parentheses indicate the film thickness in nm. In the last row, d_1 ranges from 0 to 8 nm. The substrate thickness is 500 μm.

NM material	Sample structure	Reference sample structure
Pt	Glass‖$Co_{40}Fe_{40}B_{20}$(3)‖Pt(2-16)	—
W	Glass‖$Co_{20}Fe_{60}B_{20}$(3)‖W(2-20)	Glass‖$Co_{20}Fe_{60}B_{20}$(3)‖Pt(3)
$Cu_{80}Ir_{20}$	Glass‖Fe(3)‖$Cu_{80}Ir_{20}$(2-16)‖AlO_x(3)	Glass‖Fe(3)‖Pt(4)
Cu	Glass‖$Co_{40}Fe_{40}B_{20}$(3)‖ Cu(d_1)‖Pt(3)‖Cu(8-d_1)	—

Table 2. Sample details for THz-transmission measurements, along with Drude-model fit parameters σ_{DC} and Γ, conductivity literature values σ_{DC}^{lit}, and substrate-thickness variation Δd_{sub}. Numbers in parentheses indicate the film thickness in nm. The substrate thickness is 500 μm.

Material	Sample	σ_{DC} $(10^6$ S m$^{-1})$	σ_{DC}^{lit} $(10^6$ S m$^{-1})$	Ref.	Γ $(2\pi\cdot10^{12}$ Hz)	Δd_{sub} $(\mu$m)
$Co_{40}Fe_{40}B_{20}$	Glass‖$Co_{40}Fe_{40}B_{20}$(3)‖MgO(4)	0.6	0.7	[1]	81	−0.1
Pt	Glass‖Pt(10)	3.9	5.4	[2]	51	5.8
$Co_{20}Fe_{60}B_{20}$	Glass‖$Co_{20}Fe_{60}B_{20}$(6)	0.6	—	—	25	−7.3
W	Glass‖W(10)	1.9	2.0	[3]	>100	−5.9
Fe	MgO‖Fe(3) ‖AlO_x(3)	2.7	4.0	[4]	>100	−2.2
$Cu_{80}Ir_{20}$	Glass‖$Cu_{80}Ir_{20}$(4)‖AlO_x(3)	1.0	2.0	[39]	64	−0.6

details). For these THz transmission experiments, we employ a 250 μm-thick GaP EO crystal as detector.

Note that the EO signal of the THz pulse $S(t)$ is in general not simply proportional to the transient THz electric field $E_{THz}(t)$ (figure 1(a)). Instead, it is a convolution of $E_{THz}(t)$ with the setup response function which captures the propagation and EO sampling [42, 43]. One can, in principle, retrieve the THz field $E_{THz}(t)$ from the EO signal $S(t)$ to eventually determine the dynamics of the charge current flowing inside the sample [43]. Throughout this study, however, all measurements are carried out under similar experimental conditions, thereby enabling a direct comparison of the measured raw data.

Tables 1 and 2 summarize the stacking structure of the samples used for TES and for THz-transmission measurements, respectively. Details on the sample preparation can be found in the supplementary material.

4. Results

4.1. Typical THz-emission raw data

Figure 2(a) shows typical THz-emission raw data measured from a $Co_{40}F_{40}B_{20}$(3 nm)‖Pt(3 nm) bilayer. The signal reverses almost entirely when the sample magnetization is reversed, thus confirming its magnetic origin. For all studied samples, the signal contribution being even in the sample magnetization is found to be below 5% of the signal odd in the sample magnetization. It might originate from sample imperfections such as pinned magnetic domains [44], but is not considered further as the odd signal clearly dominates. Consequently, we concentrate only on the THz signal for one orientation of sample magnetization.

We observe that the THz-signal amplitude (root mean square (RMS) of the time-domain THz signal) increases linearly with pump fluence. This finding shows that a second-order

nonlinear process in the pump laser field is operative (see figures 2(b) and S1), consistent with the linear scaling of the THz sheet charge-current density with F_{inc} as assumed in our model (see equation (1)).

We emphasize that the THz waveforms emitted from all samples exhibit similar temporal dynamics. Thus, a direct comparison of signal amplitudes (RMS) is possible.

4.2. Optical and THz characterization

To isolate the intrinsic spin-orbit-interaction-related parameters from the THz-emission signal, we first measure the optical absorptance of the pump pulse (see figure 2(c)). We note that currents arising from a pump-induced gradient can be neglected for thicknesses smaller than 20 nm because the larger penetration depth of the pump electric field and its multiple reflections result in a constant electric field along the z-direction in the sample [19].

Second, we characterize the samples by THz-transmission experiments [41]. In the thin-film limit, the THz transmission can directly be related to the metal-film conductivity, which we extract in the frequency interval from 0.5 to 5.5 THz. Details of the extraction procedure are described in the supplementary material. Note that we treat the multilayers as a parallel connection of their constituents. Therefore, the total conductance of the multilayer is given by the sum of the individual layer conductances.

We find that all metal conductivities are well described by the Drude model (see figures 2(d) and S3 and the supplementary material for details). The DC conductivity σ_{DC} and electronic current relaxation rate Γ are used as fit parameters whose values for all involved materials are given in table 2. Note that a slight variation in the substrate thickness Δd_{sub} between sample and reference THz-transmission measurements is accounted for by a phase-shift term [45, 46] of the form $\exp\left[-i\omega\left(n_2-1\right)\Delta d_{sub}/c\right]$ with the free parameter Δd_{sub} (see table 2).
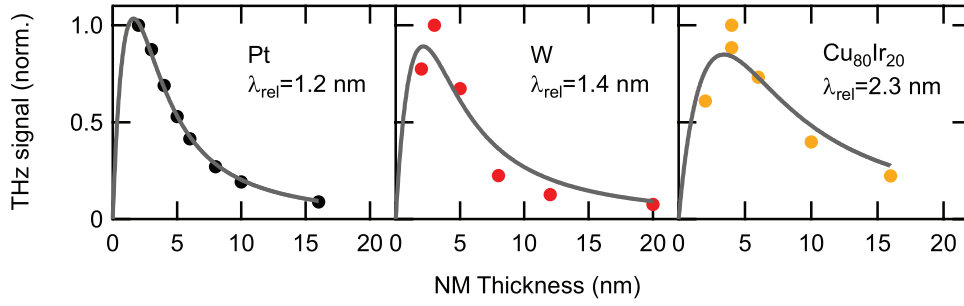
Figure 3. Thickness dependence of the THz-emission signal. THz-signal amplitude (RMS) as a function of the NM-layer thickness divided by the thickness-dependent pump absorptance for $Co_{40}Fe_{40}B_{20}(3\,nm)|Pt$ (markers in left panel), $Co_{20}Fe_{60}B_{20}(3\,nm)|W$ (center panel), and $Fe(3\,nm)|Cu_{80}Ir_{20}$ (right panel). Grey solid lines show fits based on equations (1) and (2) with the relaxation length λ_{rel} and a global amplitude as free parameters. We obtain $\lambda_{rel} = (1.2 \pm 0.1)$ nm, (1.4 ± 0.5) nm and (2.3 ± 0.7) nm for Pt, W and $Cu_{80}Ir_{20}$, respectively. For each NM material, the experimental data is normalized by the maximum amplitude.

In the following, we consider the frequency-averaged THz conductivity in which each frequency is weighted by the relative spectral amplitude of the detected THz signal. A comparison of the extracted values of σ_{DC} and literature values σ_{DC}^{lit} reveals a good agreement (see table 2). Deviations, such as those in the cases of Fe and $Cu_{80}Ir_{20}$, are most likely caused by different thicknesses [47] or crystallinity of the films. With this procedure, we have determined all parameters unrelated to the spin-to-charge conversion in the NM layer (see equations (1) and (2)).

4.3. Thickness dependence

The first spintronic key parameter to be extracted is the relaxation length λ_{rel} of the ultrafast spin current in the NM layer. To this end, we carry out measurements (see figure 3) in which the FM-layer thickness is kept constant and the NM-layer thickness is varied. The measured data are divided by the thickness-dependent pump-pulse absorptance and normalized by the maximum signal amplitude (see figures 2(c) and S2). A least-squares fit using equations (1) and (2) with the only free parameters λ_{rel} and a global amplitude, yields a λ_{rel} of (1.2 ± 0.1) nm for Pt, (1.4 ± 0.5) nm for W, and (2.3 ± 0.7) nm for $Cu_{80}Ir_{20}$ (see figure 3 and table 3). The reduced chi-squared values of the fits are 1.11, 1.04 and 1.02, respectively. We find that the values of λ_{rel} are quite insensitive to the value of the spin-current reflection amplitude at the FM/NM interface assumed in our model, thereby underlining the robustness of our analysis.

The λ_{rel} values inferred here are consistent with previous THz-emission studies on FM|Pt bilayers [19]. They agree very well with literature values from DC experiments (see table 3). The agreement is surprising as the DC experiments measure the DC spin diffusion length which does not necessarily coincide with the relaxation length of the THz spin current. The latter might be even shorter since spin flips usually occur only in a fraction of all electronic scattering events [48]. Furthermore, we find an inverse proportionality between σ_{DC} (see table 2) and λ_{rel} (see table 3). However, no correlation between the Drude scattering rate Γ and the relaxation length λ_{rel} is seen. These interesting observations will be addressed in forthcoming studies.

Table 3. Spin-Hall parameters. Spin-current relaxation length λ_{rel} along with the literature value λ_{rel}^{lit}. The table also provides the ratio of the bare THz emission signals Θ_{SH}^{raw} between a FM|NM heterostructure and the corresponding FM|Pt reference sample as well as the relative spin Hall angle Θ_{SH} extracted by our analysis correcting for sample specific parameters (see equations (1) and (2)) along with the corresponding literature value Θ_{SH}^{lit}.

| NM material	λ_{rel} (nm)	λ_{rel}^{lit} (nm)	Ref.	Θ_{SH}^{raw} (10^{-2})	Θ_{SH} (10^{-2})	Θ_{SH}^{lit} (10^{-2})	Ref.
Pt	1.2	1.1	[4]	—	—	12.0	[40]
W	1.4	<3	[17]	−5.6	−4.0	−4	[17]
$Cu_{80}Ir_{20}$	2.3	<5	[38]	3.2	1.9	2.1	[38]

4.4. Role of the FM/NM interface

To gain insights into the role of the interfacial spin-current transmission in the THz-emission experiment, we study samples with an intermediate layer with varying thickness. As the material, we choose copper because it exhibits a negligibly small SHE [32] and efficient spin current transport [49] that can be employed for spin-switching devices [50].

In detail, we measure the emitted THz signal from $Co_{40}Fe_{40}B_{20}(3\,nm)|Cu(d_1)|Pt(3\,nm)|Cu(8\,nm\text{-}d_1)$ stacks (see table 1) with d_1 ranging from 0 to 8 nm (see figure 4(a)). This choice of layer structure results in metal stacks of the same thickness and, thus, a pump-pulse absorptance of $A \approx 0.6$ and a THz outcoupling efficiency (equation (2)) which are both largely independent of d_1. Note that the Pt thickness of 3 nm is sufficient to prevent any sizeable spin-current transmission into the second copper layer (see figure 3).

Therefore, the raw data of figure 4(a) become directly comparable and provide a measure of the spin-current amplitude injected into the Pt 'detector layer'. Figure 4(b) shows that the THz-signal strength (RMS) decreases with increasing d_1. The experimental data can be very well fit (reduced chi-square value of 1.02) by a monoexponential $\propto \exp{(-d_1/\lambda_{rel})}$ with $\lambda_{rel} = (4.0 \pm 0.1)$ nm (see figure 4(b)). We note that on one hand, this value of the THz-spin-current relaxation length in Cu is substantially larger than for metals with a sizeable SHE (see figure 3). On the other hand, it is small compared to DC spin-diffusion lengths, which are on the order of 100 nm in Cu ([51]).

(a) $Co_{40}Fe_{40}B_{20}(3)|Cu(d_1)|Pt(3)|Cu(8-d_1)$

(b)
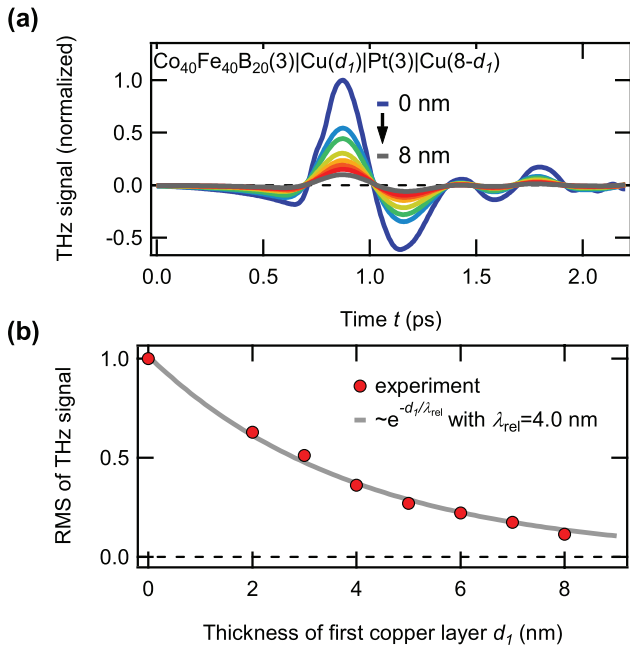
Figure 4. Role of the interface in THz-emission studies. (a) THz waveforms emitted from $Co_{40}Fe_{40}B_{20}|Cu(d_1)|Pt|Cu(8\,nm-d_1)$ structures with fixed $Co_{40}Fe_{40}B_{20}$ and Pt thicknesses of 3 nm and d_1 ranging from 0 to 8 nm. (b) THz-signal amplitudes (RMS) versus d_1 together with a single exponential fit $\propto \exp\left(-d_1/\lambda_{rel}\right)$ with $\lambda_{rel} = (4.0 \pm 0.1)$ nm. The experimental data is normalized by the maximum signal amplitude.

Interestingly, we do not observe indications of a discontinuity around $d_1 = 0$ nm. The continuous behavior suggests similar spin-current transmission efficiencies through $Co_{40}Fe_{40}B_{20}$/Pt compared to $Co_{40}Fe_{40}B_{20}$/Cu and Cu/Pt interfaces. It must be emphasized that this observation cannot be generalized and may, in contrast, strongly depend on materials and probe frequency. For example, recent gigahertz spin-pumping experiments on Co|Cu|Pt revealed a strong interface dependence of the spin-current transmission [32, 33]. Nevertheless, we note that such kind of THz-spin-current-transmission experiments could be used to characterize any FM|NM interface involving metals. To conclude, the results of figure 4 support our THz-emission model based on equations (1) and (2) assuming a minor impact of the FM|NM interface.

4.5. Extraction of the spin Hall angle

As we have determined all relevant parameters in equations (1) and (2), we can extract the relative magnitude of Θ_{SH}. Figure 5 shows raw data comparing FM|W and FM|$Cu_{80}Ir_{20}$ heterostructures with a respective Pt-capped reference sample having an identical sample architecture (see table 1). The pump-pulse absorptance of these references is 0.60 for $Co_{40}Fe_{40}B_{20}(3\,nm)|Pt(3\,nm)$ and 0.61 for $Fe(3\,nm)|Pt(4\,nm)|AlO_x(3\,nm)$.

The ratios Θ_{SH}^{raw} of the bare THz-signal amplitudes (RMS) of sample and Pt-capped reference are also displayed by figure 5. As shown in our previous work [19], Θ_{SH}^{raw} can already provide a reasonable estimate of the relative spin Hall angle Θ_{SH}. However, as shown by equation (2), this notion holds only true
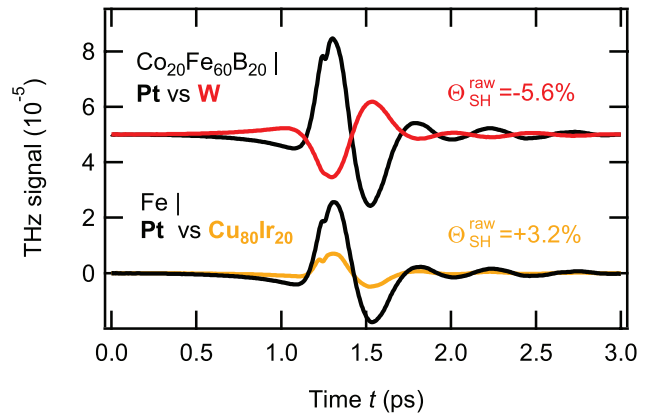
Figure 5. Comparison of THz-emission raw data from Pt, W, and $Cu_{80}Ir_{20}$. THz waveforms emitted from FM|NM structures where NM is W (red) and $Cu_{80}Ir_{20}$ (orange) in comparison to a FM|Pt reference structure with the same layer thicknesses (black curves). The values of Θ_{SH}^{raw} indicate the spin Hall angles of the respective NM materials estimated by calculating the ratios of the bare THz-signal amplitudes (RMS) and assuming a spin Hall angle of 12.0% for the Pt reference.

if the studied materials have comparable properties in terms of pump-pulse absorptance, THz conductivity and THz spin-current relaxation length (see tables 2 and 3). Our detailed analysis finally allows us to fully account for these material parameters and to eventually extract the relative Θ_{SH}. Here, Pt serves as the reference since it is by far the most studied spintronic material with $\Theta_{SH}^{Pt} = 12\%$ [40].

Table 3 is the key result of this work: It summarizes the extracted values of λ_{rel} and Θ_{SH} and compares them to the ratios Θ_{SH}^{raw} of the bare THz-signal amplitudes. When comparing to reported values of Θ_{SH}, we find very good agreement for $Cu_{80}Ir_{20}$ (2.1% in [38]). For W, the conductivity (see table 2) indicates an α crystal phase for which a Θ_{SH} of similar magnitude and sign has been reported [17, 52].

5. Discussion

Although the ratios Θ_{SH}^{raw} of the raw THz-emission signals in figure 5 already provide a reasonable estimate of the relative spin Hall angle [19], the direct comparison between Θ_{SH} and Θ_{SH}^{raw} (table 2) clearly demonstrates the need for an advanced data analysis as provided by equations (1) and (2). If only the raw data is considered, different optical and THz material properties as well as a varying λ_{rel} may have a significant impact on the extracted Θ_{SH}. For instance, variations by a factor of almost 2 occur in the case of $Cu_{80}Ir_{20}$ (see table 3).

We find good agreement between the conductivities and spintronic parameters measured by THz spectroscopy here and values measured by contact-based DC electrical schemes previously. This observation and a recent study [21] of the THz spin-Seebeck effect suggest that highly excited electrons play a minor role in the THz emission process and that thermalized electrons make the dominant contribution.

As the analysis presented here is based on our model of spin transport (equation (1)), and THz emission (equation (2)), it is important to recapitulate its assumptions and limitations. First,

J. Phys. D: Appl. Phys. **51** (2018) 364003

T S Seifert *et al*

equation (2) is only applicable for thin metal films (thickness below 20 nm), thereby ensuring a homogenous THz electric field into the depth of the metal (thin-film approximation). This condition is usually well fulfilled in practice. Second, in our analysis, THz emission by the anomalous Hall effect in the FM layer has been neglected, which, however, appears to lead to only minor corrections [26].

Finally, the spin-current transmission coefficients through the FM/NM interfaces are assumed to be approximately equal for all NM metals considered here. This assumption is supported by measurements using a Cu intermediate layer, but it is certainly important to investigate spin transmission through interfaces for a broader set of materials and interface parameters. Nevertheless, the results of this study (see table 3) clearly show that THz emission spectroscopy is a reliable tool for contactless all-optical spintronic material characterization with high sample throughput.

6. Conclusion

We present a detailed measurement and analysis scheme to establish TES as a reliable, fast and efficient all-optical method to probe spin-to-charge conversion on the femtosecond time scale. TES has several advantages: Importantly, it allows for a large sample throughput because of the relatively short measurement time which is only about 1 min for a complete THz waveform of the presented material combinations. Moreover, this all-optical and contact-free approach is very versatile as it does not require any microstructuring. It even permits the investigation of discontinuous films such as thin gold films below the percolation threshold [53]. We also present a promising experimental approach for FM/NM-interface characterization: THz-spin-current transmission measurements through a metal with negligibly small SHE. The good agreement of our measured spin-Hall parameters with literature values suggests that thermalized electrons play a significant role in the THz-emission process. Finally, our results suggest copper-iridium alloys to be promising spin-to-charge-current-conversion materials. Future TES studies will also aim at quantifying the photon-to-spin conversion efficiency and the spin-current transmission through interfaces, eventually allowing for the determination of the absolute value of spin Hall angles.

Acknowledgments

ORCID iDs

T S Seifert ● https://orcid.org/0000-0001-8163-482X
M Kläui ● https://orcid.org/0000-0002-4848-2569

References

[1] Chen Y-T and Xie S M 2012 Magnetic and electric properties of amorphous $Co_{40}Fe_{40}B_{20}$ thin films *J. Nanomater.* **2012** 29
[2] Keller S *et al* 2018 Determination of the spin Hall angle in single-crystalline Pt films from spin pumping experiments *New J. Phys.* **20** 053002
[3] Rossnagel S M, Noyan I C and Cabral C Jr 2002 Phase transformation of thin sputter-deposited tungsten films at room temperature *J. Vac. Sci. Technol.* B **20** 2047–51
[4] Rubinstein M *et al* 1988 Electrical transport properties of thin epitaxially grown iron films *Phys. Rev.* B **37** 8689
[5] Sander D *et al* 2017 The 2017 Magnetism Roadmap *J. Phys. D: Appl. Phys.* **50** 363001
[6] Prenat G *et al* 2015 Beyond STT-MRAM, spin orbit torque RAM SOT-MRAM for high speed and high reliability applications *Spintronics-Based Computing* (Cham: Springer) pp 145–57
[7] Miron I M *et al* 2011 Perpendicular switching of a single ferromagnetic layer induced by in-plane current injection *Nature* **476** 189
[8] Prenat G *et al* 2016 Ultra-fast and high-reliability SOT-MRAM: from cache replacement to normally-off computing *IEEE TMSCS* **2** 49–60
[9] Hirsch J E 1999 Spin hall effect *Phys. Rev. Lett.* **83** 1834
[10] Sinova J *et al* 2015 Spin hall effects *Rev. Mod. Phys.* **87** 1213
[11] Niimi Y and Otani Y 2015 Reciprocal spin Hall effects in conductors with strong spin–orbit coupling: a review *Rep. Progr. Phys.* **78** 124501
[12] Saitoh E *et al* 2006 Conversion of spin current into charge current at room temperature: Inverse spin-Hall effect *Appl. Phys. Lett.* **88** 182509
[13] Liu L *et al* 2011 Spin-torque ferromagnetic resonance induced by the spin Hall effect *Phys. Rev. Lett.* **106** 036601
[14] Wen Y *et al* 2017 Temperature dependence of spin-orbit torques in Cu–Au alloys *Phys. Rev.* B **95** 104403
[15] Smits F M 1958 Measurement of sheet resistivities with the four-point probe *Bell Labs Tech. J.* **37** 711–8
[16] Berger A J *et al* 2018 Inductive detection of fieldlike and dampinglike ac inverse spin-orbit torques in ferromagnet/normal-metal bilayers *Phys. Rev.* B **97** 094407
[17] Mondal S *et al* 2017 All-optical detection of the spin Hall angle in W/CoFeB/SiO_2 heterostructures with varying thickness of the tungsten layer *Phys. Rev.* B **96** 054414
[18] Kampfrath T *et al* 2013 Terahertz spin current pulses controlled by magnetic heterostructures *Nat. Nanotechnol.* **8** 256
[19] Seifert T *et al* 2016 Efficient metallic spintronic emitters of ultrabroadband terahertz radiation *Nat. Photon.* **10** 483–8
[20] Seifert T *et al* 2017 Terahertz spin currents and inverse spin Hall effect in thin-film heterostructures containing complex magnetic compounds *Spin* **7** 1740010
[21] Seifert T *et al* 2017 Femtosecond formation dynamics of the spin Seebeck effect revealed by terahertz spectroscopy *Nat. Commun.* **9** 2899
[22] Leitenstorfer A *et al* 1999 Detectors and sources for ultrabroadband electro-optic sampling: experiment and theory *Appl. Phys. Lett.* **74** 1516–8
[23] Kampfrath T, Nötzold J and Wolf M 2007 Sampling of broadband terahertz pulses with thick electro-optic crystals *Appl. Phys. Lett.* **90** 231113
[24] Ganichev S D *et al* 2002 Spin-galvanic effect *Nature* **417** 153
[25] Seifert T *et al* 2017 Ultrabroadband single-cycle terahertz pulses with peak fields of 300 kV cm^{-1} from a metallic spintronic emitter *Appl. Phys. Lett.* **110** 252402
[26] Wu Y *et al* 2017 High-performance THz emitters based on ferromagnetic/nonmagnetic heterostructures *Adv. Mater.* **29** 1603031

J. Phys. D: Appl. Phys. **51** (2018) 364003

T S Seifert *et al*

[27] Yang D *et al* 2016 Powerful and tunable THz emitters based on the Fe/Pt magnetic heterostructure *Adv. Opt. Mater.* **4** 1944–9

[28] Sasaki Y, Suzuki K Z and Mizukami S 2017 Annealing effect on laser pulse-induced THz wave emission in Ta/CoFeB/MgO films *Appl. Phys. Lett.* **111** 102401

[29] Torosyan G *et al* 2018 Optimized spintronic terahertz emitters based on epitaxial grown Fe/Pt layer structures *Sci. Rep.* **8** 1311

[30] Stamm C *et al* 2017 Magneto-optical detection of the spin Hall effect in Pt and W thin films *Phys. Rev. Lett.* **119** 087203

[31] Aeschlimann M *et al* 1997 Ultrafast spin-dependent electron dynamics in fcc Co *Phys. Rev. Lett.* **79** 5158

[32] Rojas-Sánchez J-C *et al* 2014 Spin pumping and inverse spin Hall effect in platinum: the essential role of spin-memory loss at metallic interfaces *Phys. Rev. Lett.* **112** 106602

[33] Zhang W *et al* 2015 Role of transparency of platinum-ferromagnet interfaces in determining the intrinsic magnitude of the spin Hall effect *Nat. Phys.* **11** 496

[34] Huisman T J *et al* 2017 Spin-photo-currents generated by femtosecond laser pulses in a ferrimagnetic GdFeCo/Pt bilayer *Appl. Phys. Lett.* **110** 072402

[35] Li G *et al* 2018 Laser induced THz emission from femtosecond photocurrents in Co/ZnO/Pt and Co/Cu/Pt multilayers *J. Phys. D: Appl. Phys.* **51** 134001

[36] Zhang S *et al* 2017 Photoinduced terahertz radiation and negative conductivity dynamics in Heusler alloy Co$_2$MnSn film *Opt. Lett.* **42** 3080–3

[37] Huisman T J *et al* 2016 Femtosecond control of electric currents in metallic ferromagnetic heterostructures *Nat. Nanotechnol.* **11** 455

[38] Niimi Y *et al* 2011 Extrinsic spin Hall effect induced by iridium impurities in copper *Phys. Rev. Lett.* **106** 126601

[39] Cramer J *et al* 2018 Complex terahertz and direct current inverse spin Hall effect in YIG/Cu$_{1-x}$Ir$_x$ bilayers across a wide concentration range *Nano Lett.* **18** 1064–9

[40] Obstbaum M *et al* 2014 Inverse spin Hall effect in Ni$_{81}$Fe$_{19}$/normal-metal bilayers *Phys. Rev.* B **89** 060407

[41] Duvillaret L, Garet F and Coutaz J-L 1996 A reliable method for extraction of material parameters in terahertz time-domain spectroscopy *IEEE J. Sel. Top. Quantum Electron.* **2** 739–46

[42] Leitenstorfer A *et al* 1999 Femtosecond charge transport in polar semiconductors *Phys. Rev. Lett.* **82** 5140

[43] Braun L *et al* 2016 Ultrafast photocurrents at the surface of the three-dimensional topological insulator Bi$_2$Se$_3$ *Nat. Commun.* **7** 13259

[44] Nattermann T, Shapir Y and Vilfan I 1990 Interface pinning and dynamics in random systems *Phys. Rev.* B **42** 8577

[45] Duvillaret L, Garet F and Coutaz J-L 1999 Highly precise determination of optical constants and sample thickness in terahertz time-domain spectroscopy *Appl. Opt.* **38** 409–15

[46] Krewer K L *et al* 2018 Accurate terahertz spectroscopy of supported thin films by precise substrate thickness correction *Opt. Lett.* **43** 447–50

[47] Fuchs K 1938 The conductivity of thin metallic films according to the electron theory of metals *Mathematical Proceedings of the Cambridge Philosophical Society* vol 34 (Cambridge: Cambridge University Press) (https://doi.org/10.1017/S0305004100019952)

[48] Valet T and Fert A 1996 Theory of the perpendicular magnetoresistance in magnetic multilayers *Phys. Rev.* B **48** 7099

[49] Friso Jacobus J, Filip A T and Van Wees B J 2001 Electrical spin injection and accumulation at room temperature in an all-metal mesoscopic spin valve *Nature* **410** 345

[50] Dennis I *et al* 2010 Domain-wall depinning assisted by pure spin currents *Phys. Rev. Lett.* **105** 076601

[51] Luc P, Dubois S and Fert A 1996 Perpendicular giant magnetoresistance in magnetic multilayered nanowires *J. Magn. Magn. Mater.* **159** 287–92

[52] Pai C-F *et al* 2012 Spin transfer torque devices utilizing the giant spin Hall effect of tungsten *Appl. Phys. Lett.* **101** 122404

[53] Walther M *et al* 2007 Terahertz conductivity of thin gold films at the metal-insulator percolation transition *Phys. Rev.* B **76** 125408